The Cryosphere
Discussions

Open Access

Growth of a young pingo in the Canadian Arctic observed by RADARSAT-2 interferometric satellite radar

S. V. Samsonov[1], T. C. Lantz[2], S. V. Kokelj[3], and Y. Zhang[1]

[1]Canada Centre for Mapping and Earth Observation, Natural Resources Canada, 560 Rochester Street, Ottawa, ON K1A0E4, Canada
[2]School of Environmental Studies, University of Victoria, Victoria, BC, Canada
[3]Northwest Territories Geoscience Office, Government of the Northwest Territories, Yellowknife, NWT, Canada

Correspondence to: S. V. Samsonov (sergey.samsonov@canada.ca)

TCD

9, 6395–6421, 2015

Growth of pingo observed by RADARSAT-2 InSAR

S. V. Samsonov et al.,

Title Page

Abstract | Introduction

Conclusions | References

Tables | Figures

◀ | ▶|

◀ | ▶

Back | Close

Full Screen / Esc

Printer-friendly Version

Interactive Discussion

Abstract

Advancements in radar technology are increasing our ability to detect earth surface deformation in permafrost environments. In this paper we use satellite Differential Interferometric Synthetic Aperture Radar (DInSAR) to describe the growth of a previously unreported pingo in the Tuktoyaktuk Coastlands. High-resolution RADARSAT-2 imagery (2011–2014) analyzed with the Multidimensional Small Baseline Subset (MS-BAS) DInSAR revealed a maximum $2.7\,\text{cm yr}^{-1}$ of domed uplift located in a drained lake basin. Observed changes in elevation were modeled as a $348\,\text{m} \times 290\,\text{m}$ uniformly loaded elliptical plate with clamped edge. Model results suggest that this feature is one of the largest diameter pingos in the region that is presently growing. Analysis of historical aerial photographs showed that ground uplift at this location initiated sometime between 1935 and 1951 following lake drainage. Uplift is largely due to the growth of intrusive ice, because the 9 % expansion of pore water associated with permafrost aggradation into saturated sands is not sufficient to explain the observed short- and long-term deformation rates. The modeled thickness of permafrost using the Northern Ecosystem Soil Temperature (NEST) was consistent with the maximum height of this feature and the 1972–2014 elevation changes estimated from aerial photographs, suggesting that permafrost aggradation is resulting in the freezing a sub-pingo water lens. Seasonal variation in the uplift rate seen in the DInSAR data also matches the modeled seasonal pattern in the deepening rate of freezing front. This study demonstrates that interferometric satellite radar can successfully contribute to understanding the dynamics of terrain uplift in response to permafrost aggradation and ground ice development in remote polar environments, and highlights possible application of detecting deformation of Martian landscapes. However, our DInSAR data did not show clear growth at other smaller pingos in contrast with field studies performed mainly before the 1990s. Further investigation of this apparent discrepancy may help define limitations of our processing methodology and DInSAR data.

1   Introduction

Pingos are conical ice-cored hills that grow in the permafrost environment (Mackay (1998) and references within). There are over 11 000 pingos in the world. Of these about 1350 are concentrated on the Tuktoyaktuk Coastal Plain in the western Canadian Arctic, 500 are located elsewhere in Canada, 1500 in Alaska, 6000 or more in Russia, and at least several hundred in the other parts of the world, such as Fennoscandia, Greenland, Spitsbergen, Mongolia, and Tibetan Plateau of China (Mackay, 1998; Wu et al., 2005; Grosse and Jones, 2011; Yoshikawa et al., 2013). Numerous near circular collapsed features interpreted as pingo remnants, most being of Holocene age, have been observed in former permafrost areas, such as Ireland, the United Kingdom, countries of Eastern Europe and China, suggesting the existence of permafrost in these areas more than 400 million years ago (Jin et al., 2007). Pingo-like features have also been observed on Mars using the High Resolution Imaging Science Experiment (HiRISE) camera on board the Mars Reconnaissance Orbiter (Dundas et al., 2008; Burr et al., 2009; Soare et al., 2014). Understanding the genesis, growth and collapse of pingos provides insight into the landscape forming processes associated with permafrost aggradation and ground ice development on Earth, Mars and possibly other planets.

The great majority (i.e. $\sim 98\%$) of hydrostatic or closed system pingos (Gurney, 1998; Mackay, 1998) develop in drained lake basins in association with permafrost aggradation in unfrozen saturated sandy lake sediments (Jones et al., 2011). Rapid lake drainage, caused either by coastal erosion or thermal degradation of ice wedges, exposes the lake bottom to subfreezing air temperatures (Fig. 1, Mackay, 1992). This initiates the process of permafrost aggradation into the unfrozen lake-bottom sediments. Downward aggradation of permafrost progresses at a rate inversely proportional to the square root of time (Freitag and McFadden, 1997). The water-ice phase transition produces 9 % volume expansion, i.e. $V_i = \frac{\rho_w}{\rho_i} V_w = \frac{999.97}{916.70} V_w \approx 1.09 V_w$, where ρ_w, ρ_i, V_w, and V_i are water and ice density and volume respectively. During downward

freezing of saturated sands, given free drainage, there will be little or no heave because of pore water expulsion and flow of water in the direction of lower pressure (Mackay, 1997). In a drained lake, expelled pore water typically flows to a residual pond, which is the usual site of pingo growth (Mackay, 1998). A closed system is formed when the residual pond freezes to the bottom. In this case, the pressure exerted by the ground-water flow from the surrounding lake bottom area of aggrading permafrost can heave a relatively small area, with thin permafrost beneath the residual pond, dome it up and initiate pingo growth. If the addition of water to this location exceeds the rate of downward freezing, then a pressurized, sub-pingo water lens forms and heaves the pingo upward. Freezing of the pressurized water forms intrusive ice. If the water pressure drops due to escape of water through a hydraulic fracture or a change in the ground water supply, segregated ice may form (Mackay, 1998).

Thick permafrost, sandy sediments, abundant lakes with talik (i.e. unfrozen zones) and relatively frequent lake drainage contribute to the high concentration of pingos in the Tuktoyaktuk Coastlands (Mackay, 1998). The maximum thickness of lake ice in this region is about 2 m, so lakes with greater depths are underlain by a talik (unfrozen sediments) (Mackay, 1998). The mean basal radius of pingos is about 50 m while the maximum radius is typically less than 300 m (Mackay, 1979). Their heights vary between a few meters and approximately 55 m, with a mean of 5 m (Grosse and Jones, 2011; Jones et al., 2011). Pingo basal area is typically established in the first few years of growth. Subsequently a pingo grows higher with a minimal increase in its basal area (Mackay, 1998). Pingo growth rates can vary significantly through time in response to changes in: (1) rates of ground water flow to the sub-pingo water lens, (2) release of pressurized water along hydraulic fractures and (3) variation in rates of downward freezing (Mackay, 1977, 1998). Pingo growth may continue as long as ground water continues to be supplied to the area beneath a pingo. It may take more than a thousand years for a talik to refreeze, so a pingo in the Tukotyaktuk coastlands may continue to grow for hundreds to thousands of years.

Previous studies of pingo growth and subsidence have been primarily based on annual or semi-annual field measurements of heights at benchmark locations and have required intensive field effort (Mackay, 1977, 1998). The subtle temporal changes of discrete topographic features such as pingos could not be easily detected by the early coarse resolution Synthetic Aperture Radars, such as ERS-1/2, ENVISAT or ALOS. However, availability of high resolution SAR data from the newer RADARSAT-2 satellite and advanced processing methodology allowed us to identify a very large-diameter pingo that has not been previously described in the Tuktoyaktuk Coastlands and for the first time monitor pingo growth rate with high temporal and spatial resolution over a period of four years.

2   Data and processing methodology

Historical aerial photographs, high resolution Differential Interferometric Synthetic Aperture Radar (DInSAR) data, and field measurements were used to characterize the observed feature, located in the Tuktoyaktuk Coastlands, Northwest Territories, Canada.

2.1   Historical aerial photographs

To constrain the timing of the lake drainage event and to estimate longer-term changes in elevation at this site, the following historical aerial photographs from the Natural Resources Canada Air Photo Library were analyzed: 1935 (A5023: 88R), 1951 (A12918: 092-093), 1972 (A22961: 029-030) and 2004 (A31864: 072-073). Summit Evolution Photogrammetric Workstation was used to create soft-copy stereophoto models from 1972 and 2004 aerial photographs. The scale of these images allowed us to resolve differences in height of ∼ 0.5 m. Absolute orientation was completed using a 2004 orthophoto from the Mackenzie Valley Airphoto Project supported by the Northwest Territories Centre for Geomatics and a DEM provided by the National Topo-

graphic Service, Government of Canada. To estimate the elevation at 300 (1972) and 118 (2004) locations inside the former lake basin we used Summit Evolution's stereo-plotter feature and DTM Collection tool to interface with ArcGIS and record coordinates and elevation values. This point data was interpolated to a continuous DEM for each time period using the Natural Neighbor tool in ArcGIS.

2.2 Differential Interferometric Synthetic Aperture Radar

To map the growth of this feature sixteen ascending and twenty descending Ultra-Fine 3 (U3) images with a spatial resolution of 1.6 m × 2.8 m and coverage of 20 km × 20 km (Table 1) were acquired by the RADARSAT-2 satellite between June 2011 and September 2014 over the Tuktoyaktuk Coastlands. DInSAR process-ing was performed with GAMMA software (Wegmuller and Werner, 1997). The 3 × 3 spatial averaging (i.e. multilooking) in range and azimuth directions was applied and the topographic phase was removed using 20 m DEM provided by the National To-pographic Service, Government of Canada and. From forty ascending and sixty four descending highly coherent interferograms the ascending and descending line-of-sight linear deformation rates were computed with the Small Baseline Subset (SBAS) soft-ware (Samsonov et al., 2011). Then, ascending and descending interferograms were resampled to a common grid of a reduced spatial extent that covers only the study site with the uniform spatial sampling of 10 m, and analyzed with the Multidimensional Small Baseline Subset (MSBAS) software (Samsonov and d'Oreye, 2012; Samsonov et al., 2014). This software computed vertical and horizontal deformation rates be-tween consecutive acquisitions for each pixel by simultaneously processing ascending and descending DInSAR data. Deformation time series were then reconstructed from the computed deformation rates and the mean rate was estimated by fitting a straight line to the time series. Only vertical deformation time series and the mean vertical deformation rate were used in further analysis.

2.3 Field measurements

During a field visit in August 2014 this site was surveyed using a Nikon Nivo 5.M Total Station whose position was determined using resection from two benchmarks. The position of one of these benchmarks was determined using a Trimble R4 GNSS
5   system. Post processing the data from this static survey using Natural Resources Canada's Precise Point Positioning yielded a benchmark with an orthometric height of 4.388 ± 0.001 m. This point was used to correct the elevations obtained from the Total Station survey.

3 Results: geodetic and field observations [0]

10 The Digital Elevation Model (DEM), RADARSAT-2 satellite data coverage, locations of known pingos from the Canada Base Map (GeoGratis Web Services, Natural Resources Canada) and suspected pingos visually identified in high resolution optical imagery are shown in Fig. 2.
    The observed elevated feature is located in the middle of a large, drained lake basin
15 (Fig. 3). The earliest available aerial photograph shows that in 1935 the study site was covered by a small pond (Fig. 3). By 1951, the pond was no longer visible and an area comparable with present conditions had been uplifted. This photographic evidence suggests that the growth of this feature began sometime during 1935–1951. The DEMs computed from 1972, 2004, and 2014 data (Fig. 4) show that elevation of this feature
20 gradually increased from about 8 m in 1972 to 12 m in 2014.
    The ascending and descending line-of-sight linear deformation rates (Fig. 5) were calculated with the 2σ measurement precision of 1.1 and 0.7 cm yr^{-1}, respectively. In spite of the presence of many known pingos in the area (black and brown circles in Figs. 2 and 5), deformation pattern resembling growth of pingo was only observed at
25 the study site outlined in red. This signal is particularly clear in the descending map, which was computed from a large set of sixty four interferograms. Precision of the

ascending map is lower due to the smaller number of available images, but it still fully confirms deformation signals observed in the descending map. We could not detect uplift at other known pingos because of their size comparable to the spatial sampling of deformation products (10 m) and low resolution DEM used to remove the topographic phase.

Vertical deformation time series from 2011 to 2014 calculated with MSBAS-DInSAR for the study site show maximum cumulative uplift of 9 cm over the 3.2 year time span (Fig. 6). Over this period, the maximum annual rate of 2.7 cm yr^{-1} was observed in the center of the feature (Fig. 7) and a mean uplift rate of the entire feature was 1.5 cm yr^{-1}. In order to better capture seasonal variability in the uplift rate linear and harmonic functions were simultaneously fitted to the cumulative deformation time series, and the uplift rate was estimated by differentiation of the fitted function. The modelled seasonal uplift rate reaches maximum values in August and minimum values in February. Based on these observations this near-circular feature, approximately 500 m in diameter, was interpreted as a young pingo deforming the ground surface as a result of heave generated by the presence of pressurized sub-pingo water lens and growth of intrusive and/or segregated ground ice.

4   Deformation rate modelling

The vertical deformation rate at the study site was modeled by representing the pingo-like feature as an elastic uniformly loaded elliptical plate with a clamped edge (Timoshenko and Woinowsky-Krieger, 1959):

$$\Delta w = \Delta w_0 \left(1 - \frac{X^2}{a^2} - \frac{Y^2}{b^2} \right)^2$$

$$\Delta w_0 = \frac{\Delta q}{D} \frac{1}{\left(\frac{24}{a^4} + \frac{24}{b^4} + \frac{16}{a^2 b^2} \right)}$$

$$D = \frac{E h^3}{12 \left(1 - v^2 \right)}$$

$$X = x \cos \theta + y \sin \theta$$

$$Y = -x \sin \theta + y \cos \theta \tag{1}$$

where Δw is the observed annual deformation rate, x, y and X, Y are the spatial coordinates in geodetic and rotated coordinate systems, a and b are the semi-major and semi-minor axis, θ is the tilt angle, Δq is the annual rate of change in the effective driving upward pressure of sub-permafrost pore water, E is the Young's module, h is the total thickness of the overburden and pingo ice, and v is the Poisson's ratio. Suitability of an elastic uniformly loaded circular plate model for describing the surface deformation associated with pingo growth was discussed in detail by Mackay (1987). Optimization based on simplex algorithm (Nelder and Mead, 1965) allowed estimation of the model parameters and their precision.

The best-fit model shown in Fig. 7 corresponds to an elliptical plate centered at 69.3728° N, 133.1688° W with semi-major and semi-minor axes of 348 ± 2 m and 290 ± 2 m, tilted 27 ± 3° clockwise, with magnitude of $\frac{\Delta q}{D} = 1.46 \pm 0.02 \times 10^{-10}$ m^{-2}. Assuming the total thickness of the overburden and pingo ice h ranges from 11–22 m (from NEST modeling, see below), Young's modulus E ranges 0.8–3.5 GPa (Schmeltz et al., 2002; Yang et al., 2015) and Poisson's ratio v equals 0.4, the pressure increase Δq ranges 15–540 Pa yr^{-1}, which is sufficient to uplift the ice column by 0.2–

6.0 cm yr^{-1}. The observed average uplift rate of 1.5 cm yr^{-1} is within this range. The quantity $\frac{\Delta q}{D}$ was measured with the precision of $\sim 1\%$.

5 Permafrost aggradation modeling

To approximate long-term change in the thickness of ice or ice-bonded sand produced by permafrost aggradation in an ice-cored pingo or ice-bonded sandy lake sediments, Mackay (e.g. 1979, 1998) applied a simplified Stefan solution (Ingersoll, 1954) with a one-year time step. To investigate seasonal variation and long-term rates of permafrost aggradation in the study area, we simulated the ground thermal dynamics using the Northern Ecosystem Soil Temperature (NEST) model (Zhang et al., 2003). NEST is a one-dimensional process-based transient permafrost model that considers the effects of climate, vegetation, snow, and soil conditions on ground thermal dynamics based on energy and water transfer through the soil-vegetation-atmosphere system (Zhang et al., 2003). Ground temperature is calculated by solving the one-dimensional heat conduction equation. The upper boundary condition (the ground surface or snow surface when snow is present) is determined based on the surface energy balance, and the lower boundary condition (at a depth of 120 m) is defined based on the geothermal heat flux (0.09 w m^{-2}). The thickness of the snowpack is determined based on snow density and the amount of snow on the ground (water equivalent), calculated as the cumulative difference between snowfall and snowmelt. The profile of snow density is simulated considering compaction and destructive metamorphism. Soil water dynamics are simulated considering water input (rainfall and snowmelt), output (evaporation and transpiration), and distribution among soil layers. Soil thawing and freezing, and associated changes in fractions of ice and liquid water, are determined based on energy conservation. The NEST model has been tested and applied at different scales to predict thermal conditions for areas across Canada (Zhang et al., 2005, 2006, 2008, 2012, 2014). A more detailed description of the model can be found in Zhang et al. (2003).

In this study NEST is used to model two scenarios. The first scenario (pingo scenario) models permafrost aggradation involving growth of near pure ice. This scenario provides an analogue for the growth of pingo ice over a pressurized sub-pingo water lens, which is assumed to be continuously supplied with expelled pore water from permafrost aggradation in the surrounding sediments (Fig. 1) (Mackay, 1977). In this scenario we assumed that ground materials consist of a saturated porous material with 99 % porosity to represent a growing ice core over a sub-pingo water lens. As the model was developed for terrestrial conditions, we used saturated porous material to represent sub-pingo water lens. The freezing of this water results in the growth of pingo ice. Given these assumptions and a reasonable approximation for the date of pingo inception, the modeled thickness of permafrost growth as near pure ice should approximate maximum height of the feature.

The second scenario is a hypothesis for the aggradation of permafrost into saturated sand without the development of pingo ice (non-pingo scenario). In this case ground materials consist of saturated sand with 33 %. porosity. In both scenarios we assumed that the lake drainage and permafrost aggradation began in 1940. However, since we do not know the exact date when the residual pond drained, we additionally ran the model for the two scenarios using start dates of 1930 and 1950.

The model input data of daily air temperature and precipitation were compiled from observations at Tuktoyaktuk weather station (about 10 km away from the study site and observations began in 1948) with gaps filled based on observations at Inuvik (about 115 km away from the study area). Before 1948, the climate data were filled using the data from 1960–1967. Vapor pressure was estimated using daily minimum air temperature and daily solar radiation was estimated based on latitude, day of year and diurnal temperature range (Zhang et al., 2012). For the pingo scenario, the model was initialized using a surface temperature typical for a drained lake bottom of 4 °C (Mackay, 1987). For the non-pingo scenario, the model was initialized using the climate data in 1960, a typical climate year of the area.

S. V. Samsonov et al.,

Modeling results

In the pingo scenario, the modeled thickness of permafrost was 10.7 (9.9–11.2) m by the end of 2014, which is very similar to the maximum relief of the observed feature (12 m) (Fig. 2). The modeled growth of ice thickness from 1972–2014 was 3.8 (3.6–4.3) m, which is comparable to the 4 m of vertical heave that occurred over that time period. The modeled growth rate of ice thickness during 2011–2014 was 7.4 (7.1–8.0) cm yr^{-1}, which is larger than the satellite observed maximum uplift rate (2.7 cm yr^{-1}).

In the non-pingo scenario, the modeled freezing front was at the depth of 22.6 m by the end of 2014. The 9 % volume expansion due to freezing of soil pore water to a modeled depth of 22.6 m produced 0.67 (0.61–0.71) m of uplift by the end of 2014. This is much smaller than the actual height of the observed feature (12 m) (Fig. 2). Similarly, uplift during 1972–2014 was only 0.24 (0.22–0.27) m, which is much smaller than the 4 m of vertical heave observed during that period. The maximum uplift rate during 2011–2014 was only 0.46 (0.43–0.50) cm yr^{-1}, which is much smaller than the observed maximum uplift rate of 2.7 cm yr^{-1} (Fig. 7).

The time series of the modeled permafrost aggradation rates (i.e. deepening rates of the freezing front), air temperature, and DInSAR observed uplift rates for the 2011–2014 period are shown in Fig. 8. After seven decades of permafrost aggradation the pingo (ice) and non-pingo (saturated sand) modeling scenarios showed slower deepening rate of the freezing front in February and April in comparison with higher deepening rate in July and October (Fig. 8), respectively. Due to a lag in the downward propagation of the winter cooling wave, the freezing front deepens faster in summer than winter. The 10-year difference in the model initiation time resulted in less than a 10 % difference in the depths of the freezing front and less than a month of phase shift, which are considered insignificant.

The satellite observed seasonal uplift rate reaches peak values in late August (red dashed line in Fig. 8), which coincides with the annual maximum rate of permafrost

aggradation at depth as predicted by the NEST model for the pingo scenario. Active-layer thaw in summer typically yields surface settlement in areas of permafrost terrain. These DInSAR results suggest that the seasonal pattern of satellite observed land uplift is likely driven by increased water pressure beneath the pingo and subsequent freezing of the water lens. In order to produce the observed rate of uplift during the 2011–2014 monitoring period, and a height increase of 4 m during 1972–2014, permafrost aggradation must have been accompanied by the pore water expulsion from the surrounding areas and the growth of intrusive and/or segregated ice beneath the pingo feature. It is likely that pressure conditions beneath the growing pingo feature are not always conducive to growth of intrusive ice, so that downward aggradation of permafrost beneath the pingo is yielding both lens ice and pore ice (Mackay, 1979).

6   Discussion and conclusions

The relief and size of this feature, in conjunction with observed rates of deformation suggest that uplift has occurred at least in part due to presence of a sub-pingo water lens and growth of intrusive ice. For this to occur, pore water must have been expelled from the surrounding drained lake basin by aggrading permafrost to a growing pingo. This process would buildup pore water pressure and maintain a sub-pingo water lens to enable growth of intrusive ice and heave of the ground surface, consistent with the common growth mechanism of hydrostatic pingos in Tuktoyaktuk Coastlands (Mackay, 1998).

Based on DInSAR observations, the pingo volume increase during 2011–2014 is 4672 $m^3 yr^{-1}$. If this change in volume was caused by the formation of intrusive ice by freezing of the sub-pingo water lens maintained by expelled pore water, the surrounding area has to be larger than $1.2 \times 10^6 m^2$, or ∼ 56 % of the lake basin, assuming that only 60 % × 9 % of the pore water is expelled (Mackay, 1987). This lake basin is large enough to supply such amount of water for the growth of the pingo.

Although significant attention has been given to climate warming and permafrost degradation in the arctic regions, landscape forming processes associated with permafrost aggradation and ground ice development are still very important. In spite of a large number (i.e. $> 11\,000$) of pingos on Earth their growth has never been detected by satellite radar interferometry. Previous studies of pingo dynamics were largely based on annual or semi-annual field observations performed over a long period of time (Mackay, 1998). Since the size of most pingos is comparable to the spatial resolution of early SAR sensors their dynamics could not have been easily detected by such sensors. Seasonal land cover changes (i.e. vegetation growth, snow cover) further complicated interferometric analysis. The availability of high-resolution satellite radar data and novel processing techniques, coupled with field validation provided new opportunities to study the dynamics of pingos and other permafrost processes associated with ground ice development and degradation at high temporal and spatial resolutions.

Historical aerial photographs, field measurements and modeling suggest that the satellite detected feature is an actively growing pingo that developed over a residual pond in a large drained lake basin. Uplift of the ground at this location initiated sometime between 1935 and 1951 following lake drainage and is caused at least in part by the growth of intrusive ice, because the 9 % expansion of pore water during normal permafrost aggradation is not sufficient to explain the observed short- and long-term deformation rates. Thermal modeling of permafrost growth involving the freezing of a water lens indicated that modeled thickness of ice growth from 1940 to 2014 is comparable with the maximum height of this feature. Similarly, the modeled thickness of ice growth from 1972 to 2014 is comparable with changes in elevation of the feature estimated from aerial photographs. Seasonal pattern of variation in the uplift rate seen in the DInSAR data also matches the modeled seasonal change in the deepening rate of freezing front. Seasonal changes in the rate of pingo ice growth have also been observed in alternating clear and bubble bands in pingo ice (Mackay, 1990). The model of a pingo as an elastic uniformly loaded elliptical plate with clamped edge provided a good fit to the observed feature. The location, and semi-major and semi-minor radii

of the modeled feature are 69.3728° N, 133.1688° W, 348 ± 2 m and 290 ± 2 m. Our observations indicate that this pingo is one of the largest (diameter) actively growing pingos presently known. DInSAR could also be used for studying other known pingos, pingo remnants and pingo-like features observed on Mars. Future monitoring of this and other ground-ice related landforms by interferometric satellite radar, which can yield high resolution spatial and temporal data will contribute to a better understanding of permafrost related processes, including the impact of climate change.

This analysis of ground deformation in the Tuktoyaktuk Coastlands (Fig. 5) only shows active deformation, resembling pingo growth, at one single site. However, earlier field measurements performed by Mackay (1998) showed that many of the smaller pingos in the Tuktoyaktuk Coastlands are actively growing. The majority of RADARSAT-2 interferograms used in this study were contaminated by various sources of noise, including decorrelation caused by seasonal changes and snow cover, atmospheric disturbances and residual orbital ramps, which resulted in reduced precision. However, a few interferograms acquired in ideal conditions (i.e. small spatial baseline, frozen ground, no snow) were of an exceptionally high quality. In these interferograms no active deformation processes of similar spatial extent and magnitude were observed except for the pingo studied here. The discrepancy between long-term field measurements and these results is likely caused by the inability of our processing methodology to resolve deformation at smaller spatial scales. The DInSAR spatial resolution can be improved by using high-resolution DEM for removing the topographic phase.

References

Burr, D., Tanaka, K., and Yoshikawa, K.: Pingos on Earth and Mars, Planet. Space Sci., 57, 541–555, 2009. 6397

Dundas, C., Mellon, M., McEwen, A., Lefort, A., Keszthelyi, L., and Thomas, N.: HiRISE observations of fractured mounds: Possible Martian pingos, Geophys. Res. Lett., 35, doi:10.1029/2007GL031798, 2008. 6397

Freitag, D. and McFadden, T.: Introduction to Cold Regions Engineering, ASCE Publications, 1997. 6397

Grosse, G. and Jones, B. M.: Spatial distribution of pingos in northern Asia, The Cryosphere, 5, 13–33, doi:10.5194/tc-5-13-2011, 2011. 6397, 6398

Gurney, S.: Aspects of the genesis and geomorphology of pingos: perennial permafrost mounds, Prog. Phys. Geogr., 22, 307–324, 1998. Ingersoll, L. R., Zobel, O. J., and Ingersoll, A. C.: Heat conduction with engineering, geological, and other applications. University of Wisconsin Press, Madison, 325 pp., 1954. 6397

Jin, H., Chang, X., and Wang, S.: Evolution of permafrost on the Qinghai-Xizang (Tibet) Plateau since the end of the late Pleistocene, J. Geophys. Res., 112, F02S09, doi:10.1029/2006JF000521, 2007. 6397

Jones, B., Grosse, G., Hinkel, K., Arp, C., Walker, S., Beck, R., and Galloway, J.: Assessment of pingo distribution and morphometry using an IfSAR derived digital surface model, western Arctic Coastal Plain, Northern Alaska, Geomorphology, 138, 1–14, 2011. 6397, 6398

Mackay, J.: Pulsating pingos, Tuktoyaktuk Peninsula, N.W.T., Can. J. Earth Sci., 14, 209–222, 1977. 6398, 6399, 6405

Mackay, J.: Pingos of the Tuktoyaktuk Peninsula Area, Northwest Territories, Geographie Physique et Quaternaire, 33, 3–61, 1979. 6398, 6404, 6407

Mackay, J.: Some mechanical aspects of pingo growth and failure, western Arctic coast, Canada, Can. J. Earth Sci., 24, 1108–1119, 1987. 6403, 6405, 6407

Mackay, J.: Seasonal growth banks in pingo ice, Can. J. Earth Sci., 27, 1115–1125, 1990. 6408

Title Page

Abstract | Introduction

Conclusions | References

Tables | Figures

|◀ | ▶|

◀ | ▶

Back | Close

Full Screen / Esc

Printer-friendly Version

Interactive Discussion

Mackay, J.: Arctic ecosystems in semi-arid regions: Implications for resource management, in: chap. Lake stability in an ice-rich permafrost environment: examples from the western Arctic coast, NHRI Symposium Series 7, Environment Canada, Saskatoon, Sask., 1–25, 1992. 6397

Mackay, J.: A full-scale field experiment (1978–1995) on the growth of permafrost by means of lake drainage, western Arctic coast: a discussion of the method and some results, Can. J. Earth Sci., 34, 17–33, 1997. 6398

Mackay, J.: Pingo growth and collapse, Tuktoyaktuk Peninsula Area, Western Arctic Coast, Canada: A long-term field study, Geographie Physique et Quaternaire, 3, 271–323, 1998. 6397, 6398, 6399, 6404, 6407, 6408, 6409, 6414

Nelder, J. and Mead, R.: A simplex method for function minimization, Computat. J., 7, 308–313, 1965. 6403

Samsonov, S. and d'Oreye, N.: Multidimensional time series analysis of ground deformation from multiple InSAR data sets applied to Virunga Volcanic Province, Geophys. J. Internat., 191, 1095–1108, 2012. 6400

Samsonov, S., van der Koij, M., and Tiampo, K.: A simultaneous inversion for deformation rates and topographic errors of DInSAR data utilizing linear least square inversion technique, Comput. Geosci., 37, 1083–1091, 2011. 6400

Samsonov, S., d'Oreye, N., González, P., Tiampo, K., Ertolahti, L., and Clague, J.: Rapidly accelerating subsidence in the Greater Vancouver region from two decades of ERS-ENVISAT-RADARSAT-2 DInSAR measurements, Remote Sens. Environ., 143, 180–191, 2014. 6400

Schmeltz, M., Rignot, E., and MacAyea, D.: Tidal flexure along ice-sheet margins: comparison of InSAR with an elastic-plate model, Ann. Glaciol., 34, 202–208, 2002. 6403

Soare, R., Conway, S., Dohm, J., and El-Maarry, M.: Possible open-system (hydraulic) pingos in and around the Argyre impact region of Mars, Earth Planet. Sc. Lett., 398, 25–36, 2014. 6397

Timoshenko, S. and Woinowsky-Krieger, S.: Theory of Plates and Shells, in: Engineering Societies Monographs, McGraw-Hill Book Company, Inc., New York-Toronto-London, 1959. 6402

Wegmuller, U. and Werner, C.: GAMMA SAR processor and interferometry software, in: The 3rd ERS symposium on space at the service of our environment, Florence, Italy, 1997. 6400

Wu, Z., Barosh, P., Hu, D., Wu, Z., Peisheng, Y., Qisheng, L., and Chunjing, Z.: Migrating pingos in the permafrost region of the Tibetan Plateau, China and their hazard along the Golmud-Lhasa railway, Eng. Geol., 79, 267–287, 2005. 6397

Title Page

Abstract | Introduction

Conclusions | References

Tables | Figures

◄◄ | ►►

◄ | ►

Back | Close

Full Screen / Esc

Printer-friendly Version

Interactive Discussion

Yang, Z., Still, B., and Ge, X.: Mechanical properties of seasonally frozen and permafrost soils at high strain rate, Cold Reg. Sci. Technol., 113, 12–19, 2015. 6403

Yoshikawa, K., Sharkhuu, N., and Sharkhuu, A.: Groundwater hydrology and stable isotope analysis of an open-system pingo in Northwestern Mongolia, Permafrost Periglac. Process., 24, 175–183, 2013. 6397

Zhang, Y., Chen, W., and Cihlar, J.: A process-based model for quantifying the impact of climate change on permafrost thermal regimes, J. Geophys. Res.-Atmos., 108, 4695, doi:10.1029/2002JD003354, 2003. 6404

Zhang, Y., Chen, W., Smith, S., Riseborough, D., and Cihlar, J.: Soil temperature in Canada during the twentieth century: complex responses to atmospheric climate change, J. Geophys. Res., 110, D03112, doi:10.1029/2004JD004910, 2005. 6404

Zhang, Y., Chen, W., and Riseborough, D.: Temporal and spatial changes of permafrost in Canada since the end of the Little Ice Age, J. Geophys. Res., 111, D22103, doi:10.1029/2006JD007284, 2006. 6404

Zhang, Y., Chen, W., and Riseborough, D.: Disequilibrium response of permafrost thaw to climate warming in Canada over 1850–2100, Geophys. Res. Lett., 35, L02502, doi:10.1029/2007GL032117, 2008. 6404

Zhang, Y., Li, J., Wang, X., Chen, W., Sladen, W., Dyke, L., Dredge, L., Poitevin, J., McLennan, D., Stewart, H., Kowalchuk, S., Wu, W., Kershaw, G. P., and Brook, R.: Modelling and mapping permafrost at high spatial resolution in Wapusk National Park, Hudson Bay Lowlands, Can. J. Earth Sci., 49, 925–937, 2012. 6404, 6405

Zhang, Y., Olthof, I., Fraser, R., and Wolfe, S. A.: A new approach to mapping permafrost and change incorporating uncertainties in ground conditions and climate projections, The Cryosphere, 8, 2177–2194, doi:10.5194/tc-8-2177-2014, 2014. 6404

Title Page

Abstract | Introduction

Conclusions | References

Tables | Figures

|◄ | ►|

◄ | ►

Back | Close

Full Screen / Esc

Printer-friendly Version

Interactive Discussion

**Table 1.** RADARSAT-2 Ultra-Fine 3 (U3) Synthetic Aperture Radar images used in this study, θ is azimuth and ϕ is incidence angle, N is number of images and M is number of interferograms computed for each data set. Time series span 19 June 2011–7 September 2014 interval when both ascending and descending data are available.

DInSAR set	Orbit	Coverage	$\theta°$	$\phi°$	N	M
RADARSAT-2, U3	asc	20110612-20140924	344	32	16	40
RADARSAT-2, U3	dsc	20110619-20140907	−165	32	20	64
Total:		20110619-20140907			34	102
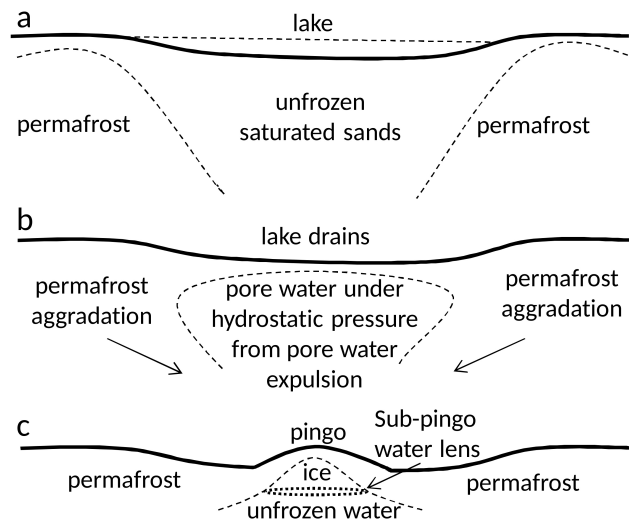
Figure 1. Growth of close system pingo (modified from Mackay, 1998): **(a)** lake underlain by basin of unfrozen saturated sands; **(b)** lake after rapid drainage, permafrost aggradation, pore water expulsion, hydrostatic pressure increase beneath residual pond with thin layer of permafrost; **(c)** growing pingo underlain by sub-pingo water lens.
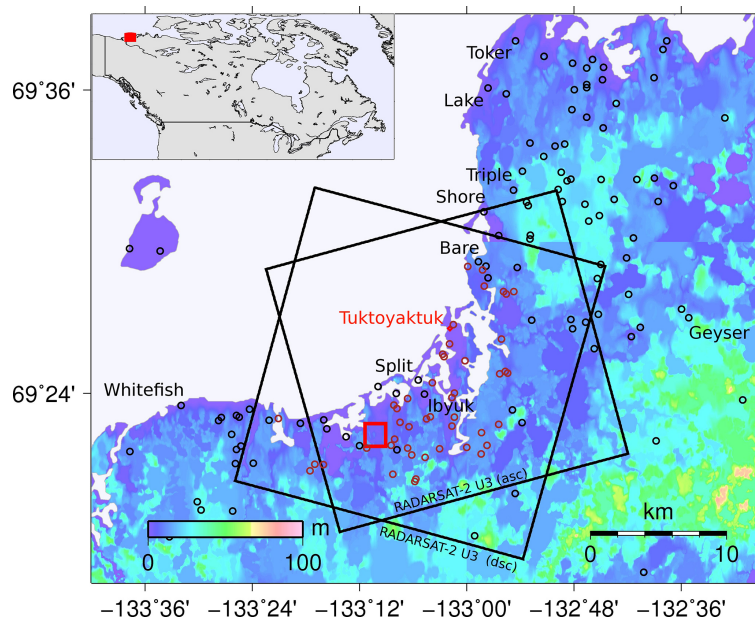
Figure 2. Study site located in Northwest Territories, Canada is outlined in red. Background is 90 m resolution Digital Elevation Model (GeoGratis Web Services, Natural Resources Canada). Ascending and descending RADARSAT-2 Ultra-fine 3 (U3) frames are outlined in black. Black circles show locations of known pingos from Canada Base Map (GeoGratis Web Services, Natural Resources Canada). Brown circles show locations of suspected pingos visually identified in high resolution optical imagery. Names of known pingos are shown in black. Extent in top-left corner shows location of site in North America.

Title Page

Abstract | Introduction

Conclusions | References

Tables | Figures

|◀ | ▶|

◀ | ▶

Back | Close

Full Screen / Esc

Printer-friendly Version

Interactive Discussion

Full Screen / Esc
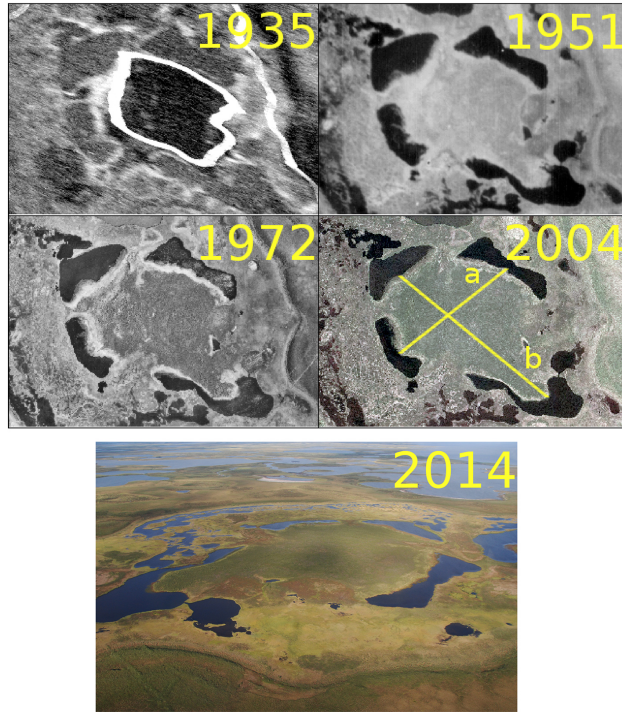
Figure 3. Top panel: historical aerial photographs of study site (National Air Photo Library, Natural Resources Canada) from 1935, 1950, 1972, and 2004 showing that the study site was occupied by a pond in 1935. For reference length of a is 560 m and length of b is 770 m. Bottom panel: photograph of study site taken in August 2014 from helicopter (viewing from east).

Figure 4. Elevation ($> 5\,\text{m}$) in 1972 and 2004 from stereo-photo analysis and Total Station surveys. Background is average radar back-scatter intensity.

Full Screen / Esc
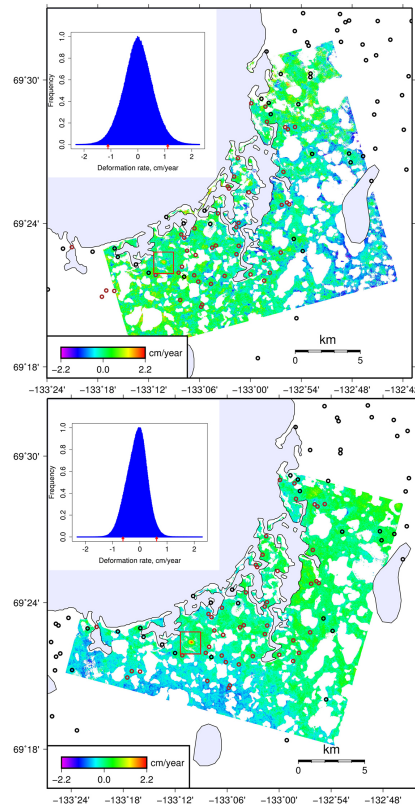
Figure 5. Line-of-sight linear deformation rate during 2011–2014 period computed from ascending (top panel) and descending (bottom panel) RADARSAT-2 U3 imagery. Study site is outlined in red. Black circles show locations of known pingos from Canada Base Map (GeoGratis Web Services, Natural Resources Canada). Brown circles show locations of suspected pingos visually identified in high resolution optical imagery. Extents in top-left corner show deformation rate histograms with red arrows marking 95 % confidence interval.
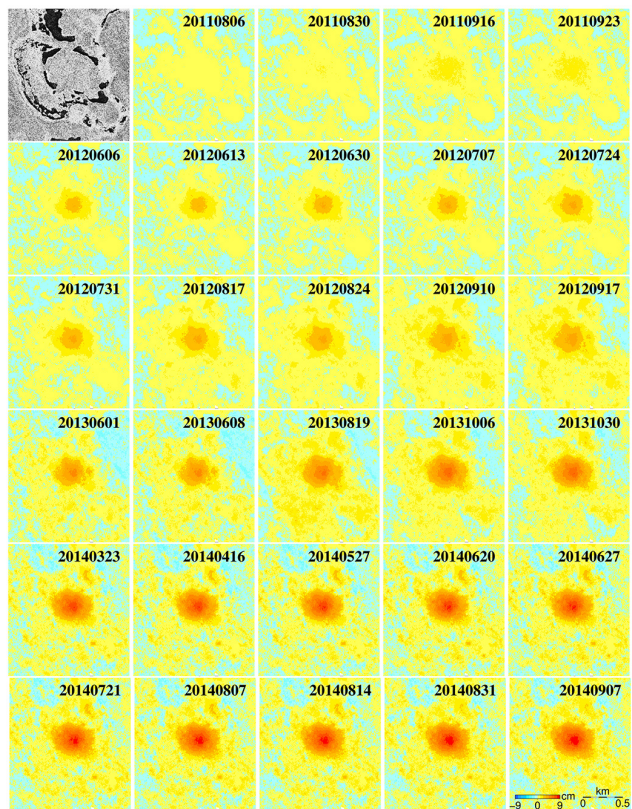
Figure 6. Time series of vertical ground deformation spanning 6 August 2011–7 September 2014 computed from ascending and descending RADARSAT-2 data using Multidimensional Small Baseline Subset (MSBAS) technique. Gray image shows average radar back-scatter intensity.
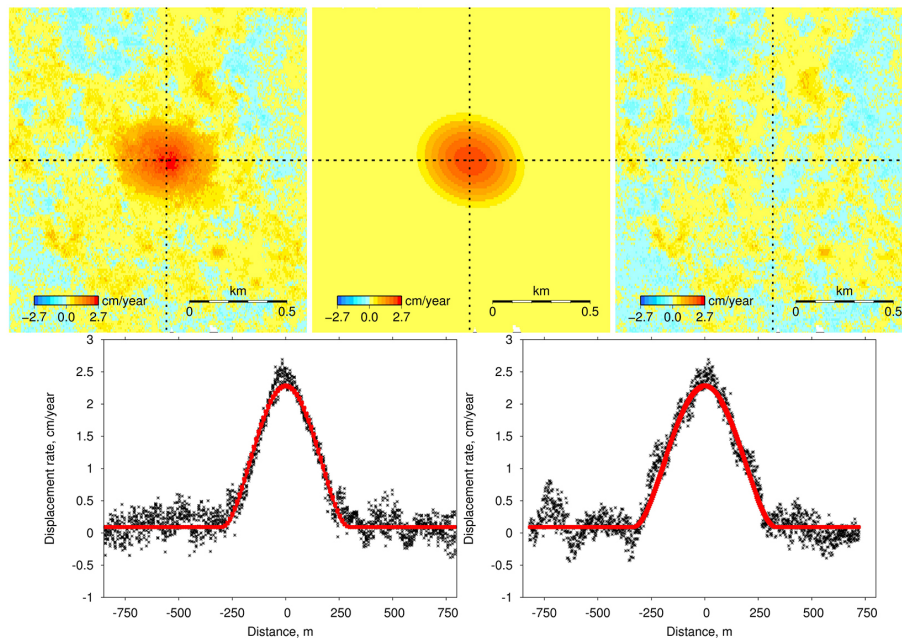
Figure 7. Top panels: observed data, model and residual of vertical linear deformation rate. Best fit model corresponds to ellipse located at 69.3728° N, 133.1688° W with semi-major and semi-minor radii of 348 ± 2 m and 290 ± 2 m, tilted $27 \pm 3°$ clockwise, with magnitude of $\frac{\Delta q}{D} = 1.46 \pm 0.02 \times 10^{-10}$ m^{-2}. Bottom panels: latitudinal and longitudinal profiles across uplifting area. Observed data is plotted in black, modeled data is plotted in red.
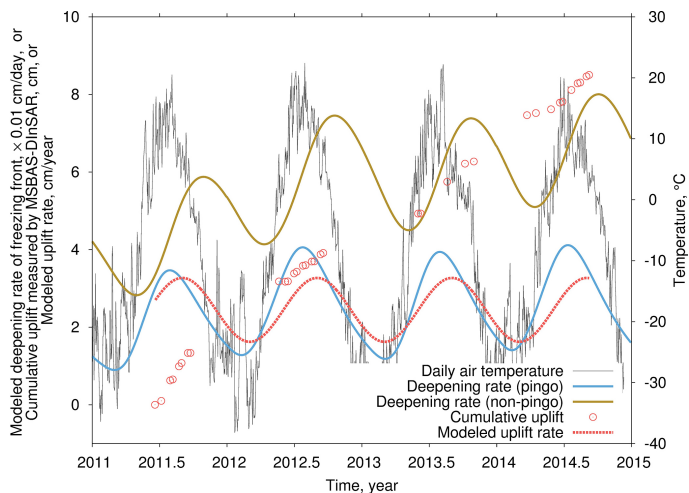
Figure 8. Modeled deepening rate of freezing front for pingo (blue line) and non-pingo (brown line) scenarios assuming lake drained in 1940, vertical ground deformation time series for area experiencing maximum uplift (red circles), modeled uplift rate (red dashed line), and mean daily air temperature observed at Tuktoyaktuk weather station located 10 km north-east from study site (gray blue). Acceleration of uplift is observed in August when deepening rate of freezing front is largest and air temperature reaches annual maximum.